TELLUS

On the climate forcing consequences of the albedo continuum between cloudy and clear air

By ROBERT J. CHARLSON[1], ANDREW S. ACKERMAN[2*], FRIDA A-M. BENDER[3],
THEODORE L. ANDERSON[1*] and ZHAOYAN LIU[4],   [1]*Department of Atmospheric Sciences,*
University of Washington, Seattle, WA 98195, USA; [2]*NASA Goddard Institute for Space Studies, New York, NY 10025,*
USA; [3]*Department of Meteorology, Stockholm University, Stockholm, Sweden;* [4]*National Institute of Aerospace,*
Hampton, VA 23666, USA

ABSTRACT

It has been long understood that the partly cloudy atmosphere manifests a continuum of states between the end members 'clear' and 'cloud.' Nevertheless, many research methods are premised on a dichotomy of states—for example, those that use 'cloud cover' or 'cloud-clearing.' Here we consider the consequences of this practice for studies of aerosol-climate effects. Aerosols affect the Earth's energy budget primarily by affecting albedo; therefore, we explore the nature of albedo variability in the partly cloudy marine boundary layer on scales down to a few tens of metres. We employ two diagnostic tools: a cloud resolving model and an albedo proxy derived from high altitude lidars. We show that a continuum of albedo values results from indeterminate and variable combinations of hydrated aerosol and wispy (including subvisible) clouds. Two consequences arise. First, cloud-clearing schemes employed by different observational methods are mutually inconsistent and are sensitive to concentrations of unactivated aerosol particles. Second, aerosol radiative forcing (the sensitivity of overall albedo to changes in aerosol concentration) is inaccurately calculated as the average of clear and overcast conditions. Together, these results imply that dividing the aerosol forcing problem into 'direct' and 'indirect' components may lead to substantial errors.

1. Introduction

Climate stability requires a balance of absorbed solar radiation and emitted long-wave radiation by the Earth system. Accumulation of greenhouse gases such as CO_2 influence long-wave emission and are central to the question of human-induced global warming. Planetary albedo controls the absorption of solar radiation and, in turn, is largely controlled by condensed atmospheric water in the form of clouds. Clouds typically have a distinct visible boundary where air becomes supersaturated with respect to water vapour (e.g. at cloud base Howell, 1949). This phenomenon is explained by the thermodynamics of cloud droplet activation (Köhler, 1921, 1936) and gives rise to the notion of 'clear' and 'cloudy' air being distinct entities.

Separating the atmosphere into clear and cloudy regimes has long been a basic premise in studies of the atmospheric contributions to albedo. These include efforts to quantify cloud radiative forcing (Ramanathan et al., 1989), to simulate global climate change (Collins et al., 2004), and to separately quan-

tify *direct* and *indirect* aerosol forcings of climate (Junge, 1975; Charlson et al., 1991, 1992). This clear-cloudy dichotomy also is embedded in meteorological observations such as fractional cloud cover and is the starting point for essentially all analyses of ground-based radiometry and sun-photometry (e.g. Smirnov et al., 2000), satellite radiometry (e.g. Trepte et al., 1999; Martins et al., 2002; Zhao et al., 2005), and lidar measurements (e.g. Mattis et al., 2004; Matthias et al., 2004). These examples underscore the long-established practice of treating clouds as discrete objects, rather than as visible manifestations of a continuum of thermodynamic states.

Multiple lines of evidence exist that call into question the degree to which clear and cloudy skies can be separated, especially under conditions of scattered-to-broken sky cover. This issue has been explored extensively in considerations of remote sensing of cloud cover or cloud properties (Wielicki and Welch, 1986; Considine et al., 1997), in the analysis of satellite imagery (Wielicki and Parker, 1992) and in the development of model parametrizations of clouds (Harshvardhan et al., 1994; Barker et al., 1996). Ideally, the probability density function (PDF) of cloud optical depth could be used as an objective index, wherein fully separable clear and cloudy air would have a maximum for 'clear air' and another maximum for 'cloud,'

*Corresponding authors.
e-mail: andrew.ackerman@nasa.gov, tadand@atmos.washington.edu

with a minimum or zero probability in between. This region of low probability has in fact been inferred from transmission measurements in the Antarctic sea-ice zone and it has been dubbed the 'Köhler gap' (Fitzpatrick and Warren, 2005) under the assumption that it arises from the highly non-linear phenomenon of cloud droplet activation. However, in almost all cases of fractional sky cover, rather than displaying separate peaks, the PDFs have a single peak at zero optical depth. This implies that fragments of clouds exist down to very small optical depths, indeed, down to optical depths less than that of the aerosol seen in clear air. The result is a continuum of cloud optical depths, which in turn causes a continuum of albedos of scattered-to-broken clouds.

In spite of these findings, attempts to separate clear and cloudy skies have seemingly increased over the past decade since the above revelations appeared. Almost all atmospheric remote sensing programs have established a cloud-clearing protocol for selecting clear skies and/or a cloud masking protocol for quantifying cloud amounts or cloud properties. One major exception is the Clouds and the Earth's Radiant Energy System (CERES) and Earth Radiation Budget Experiment (ERBE) protocols that use cloud detection algorithms only for the purpose of selecting angular distribution models (ADMs) for converting measured radiances to fluxes. The resulting fluxes are less dependent on the accuracy of derived cloud cover than on the consistency of the scene identification when viewed from different angles. Essentially all other observational approaches use cloud identification algorithms as the first step in separately quantifying the properties of clear versus cloudy skies. A typical example is the estimation of aerosol optical depth in the subset of Aerosol Robotic Network (AERONET) observations that are selected as being 'clear' (Kaufman and Koren, 2006). Remote sensing approaches to separating *clear* and *cloudy* pixels are generally based on the spatial or temporal variability of transmitted solar radiation (e.g. AERONET), reflected solar radiation (e.g. Moderate Resolution Imaging Spectroradiometer [MODIS]), or reflected laser radiation [e.g. Geoscience Laser Altimeter System (GLAS) or Cloud-Aerosol Lidar and Infrared Pathfinder Satellite Observations (CALIPSO)].

Herein we use two new approaches in order to assess the realism and the potential impacts of the conventional assumption that the atmosphere can be divided into clear and cloudy regimes. We do this by examining albedo or proxy-albedo data from a high resolution (cloud-resolving) model, high resolution remote observations (airborne lidar), and lower resolution satellite-borne lidar. Despite their differences, the distributions of albedo values consistently suggest that the atmosphere does not separate into distinct clear and cloudy cases, in agreement with the earlier findings. But, beyond what was known from the previous studies, both the lidar observations and cloud-resolving model allow new inferences of the causes of the observed continuum and its sensitivity to added aerosol.

To set the context for this analysis, consider the 'conventional expression' (Cess, 1976) for planetary albedo:

$$A = (1 - F_{\text{cloudy}})A_{\text{clear}} + F_{\text{cloudy}}A_{\text{cloudy}}, \qquad (1)$$

where A is albedo, F_{cloudy} is the fractional cloud cover and A_{clear} and A_{cloudy} are the albedos of clear and cloudy areas, respectively. The lidar and model data we consider allow examination of just the atmospheric contribution to albedo, by omitting surface reflection. This would be an accurate description of reality if the surface albedo were zero, which is approximately true for much of the global ocean. Application of eq. (1) would be straightforward if the PDF of atmospheric albedo displayed a bimodal form, with a low albedo mode for clear skies, a higher albedo mode for cloudy skies, and a region of low probability in between. In the data sets examined below, it appears that the clear-air mode is broadened by optically thick aerosol and the cloud mode is broadened by optically thin or wispy clouds, causing this gap region to largely or completely disappear.

2. Inseparability of clear and cloudy skies under partial cloud cover

In order to simulate the albedos of clear and cloudy air, we examine albedo PDFs derived from large-eddy simulations (LES) of the marine boundary layer, at a horizontal resolution of 50–70 m (Ackerman et al., 2004). Meteorological inputs to the LES are idealizations of measurements acquired in three field experiments (as described in Appendix A). Nominal cloud cover is 7% for the BOMEX trade cumulus simulation, 100% for the ASTEX stratocumulus simulation, and 54% for the ATEX trade cumulus simulation (here we define cloud cover as the time averaged fraction of columns with water mass mixing ratio in activated drops exceeding 0.05 g kg^{-1} in at least one grid cell). We assume an underlying surface albedo of zero in order to isolate the atmospheric contribution to albedo. When plotting the PDFs, we define the variable on the ordinate as df/dA (where f is the normalized cumulative frequency of albedo $> A$). This convention best depicts what albedo values are controlling the area-weighted mean albedo. An alternate convention that instead depicts what controls total reflected light over the domain is discussed in Appendix B.

Figures 1a and b depict the distribution of atmospheric albedo for the marine boundary layer under nearly clear (BOMEX) and overcast (ASTEX) conditions. Figure 1c shows the PDF for half of their sum, which would correspond to roughly 50% cloud cover. This simple picture—two widely separated modes such that quantification of all terms in eq. (1) would be straightforward—results from aggregating overcast and nearly clear conditions.

A very different picture emerges from model simulations of the partly cloudy (ATEX) case, characterized by roughly 50% cloud cover. Instead of two distinct modes, Fig. 1d shows a broad
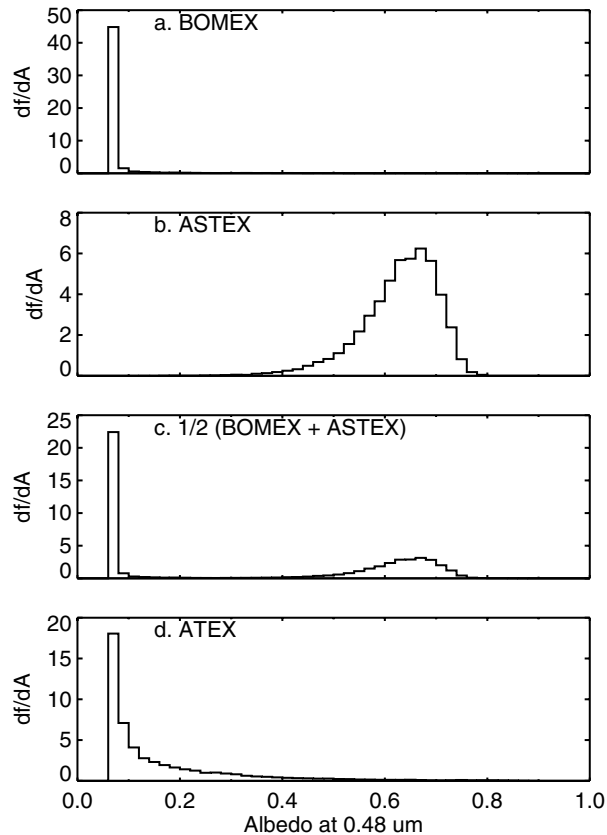
Fig. 1. Albedo PDFs from large-eddy simulations of trade cumulus and stratocumulus clouds. *A* is albedo at 480 nm for model columns (50 to 67 m wide), and *f* is the normalized cumulative frequency of columns with albedo > *A*. Simulations are based on meteorological conditions measured during field projects: (a) BOMEX trade cumulus, with simulated cloud cover ~10%; (b) ASTEX stratocumulus, in which the simulated clouds are overcast; and (d) ATEX trade cumulus, with simulated cloud cover ~50%; (c) average of the BOMEX and ASTEX fields. Total particle concentration is fixed at 150 cm^{-3} for all of the simulations. Further details provided in the text.

continuum of albedo values. For this case, therefore, it might be problematic to separate the albedo contributions of the clear and cloudy portions of the domain, as called for in eq. (1). In the following sections, we will use lidar data to assess whether this simulated albedo distribution for partly cloudy skies is realistic.

3. Lidar reflectivity as a proxy for albedo

3.1. Definition and comparison with other measurements

We introduce *lidar reflectivity*, R_L, as a diagnostic variable. It is useful because (i) it is readily and accurately derived from high-altitude, downward-looking lidar, (ii) it provides better horizontal resolution than broadband flux measurements operated from the same altitude and (iii) it allows observational assessment of the contribution of the atmosphere and its various layers to plan-

etary albedo, independent of surface albedo. From an operational standpoint, R_L is simply the vertical integral of the calibrated, range-corrected, lidar signal,

$$R_L(\lambda) = C(\lambda) \int_{z_1}^{z_2} X(\lambda, z) \mathrm{d}z = \int_{z_1}^{z_2} \beta'(\lambda, z) \mathrm{d}z, \qquad (2)$$

where $C(\lambda)$ is the lidar calibration constant at laser wavelength λ, $X(\lambda,z)$ is the background-subtracted, energy-normalized, range-corrected lidar return signal corresponding to altitude z, and $\beta'(\lambda,z)$ is the so-called attenuated backscatter coefficient (Platt, 1973). To characterize the entire column, z_1 would be the bottom and z_2 the top of the atmosphere. Henceforth we omit the wavelength designation for simplicity.

Intuitively, the quantity R_L represents a type of reflectivity, for it corresponds to the fraction of laser irradiance that is backscattered by the atmosphere and returned to the sensor. With this in mind, we associate the physical meaning of R_L with the reflectivity of the atmosphere at a scattering angle of 180°, R_π,

$$R_L = R_{\pi,\mathrm{dir}} + f R_{\pi,\mathrm{diff}}, \qquad (3)$$

where $R_{\pi,\mathrm{dir}}$ is direct 180° reflectivity, $R_{\pi,\mathrm{diff}}$ is diffuse 180° reflectivity (i.e. arising from multiple scattering), and f is the fraction of $R_{\pi,\mathrm{diff}}$ that is actually sensed by the lidar for a given instrumental geometry and atmospheric state. The reason for the parameter f is that multiply scattered photons migrate horizontally and therefore, may migrate outside the field of view of the lidar detector.

Note that the R_L parameter used herein is essentially the same as the 'integrated attenuated backscatter' parameter introduced by Platt (1973) and discussed frequently in the lidar literature. The critical difference is that previous lidar studies have sought to minimize and correct for multiple-scattering effects, in order to focus on direct backscatter and derive extinction optical depth. In contrast, we are interested in sampling *all* of the multiply scattered radiation emerging from the top-of-atmosphere in the 180° backscatter direction, for the purpose of characterizing atmospheric reflectivity.

R_L consists of a radiance divided by an irradiance and therefore has units of sr^{-1}. Planetary albedo, A, on the other hand, is the reflected flux divided by the incident irradiance—a dimensionless ratio. To resolve this discrepancy, we multiply R_L by π steradians, which is the radiance-to-flux conversion factor for the simple case of isotropic scattering. We do not contend that the quantity πR_L constitutes an accurate measure of broadband, planetary albedo. Rather, we propose that variations in these two quantities are likely to be closely related under some conditions, such that πR_L can provide diagnostic information on the nature and causes of albedo variability. More specifically, in proposing that πR_L can serve as a diagnostic proxy for A, we are making three assumptions: (i) that R_L approximates R_π, which will be true for optically thin atmospheres, where $R_{\pi,\mathrm{diff}}$ is small, or whenever f is near unity, (ii) that 180° reflectivity correlates with reflected flux, which will be true to the extent that variations in
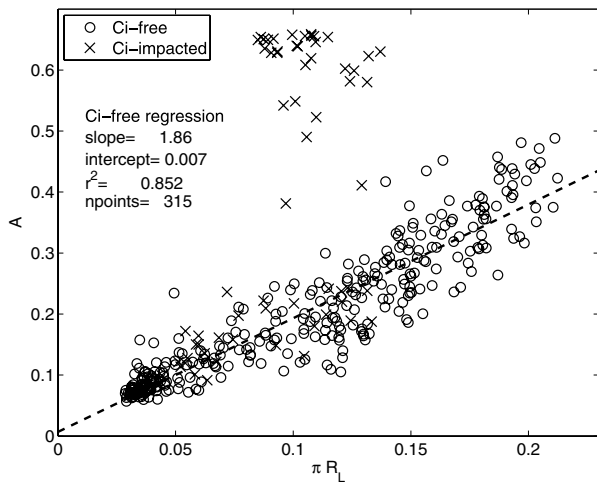
Fig. 2. Broadband albedo, A, from CERES versus the collocated, lidar-derived albedo proxy data, πR_L, from the Cloud-Aerosol Lidar with Orthogonal Polarization (CALIOP). CALIOP data within each CERES pixel have been averaged. The CERES pixel size is about 20 km. CALIOP samples only a small fraction (about 0.05%) of each pixel, so the relationship is expected to be noisy whenever subpixel variability is high. The regression is based on cirrus-free pixels only (as defined by the CALIOP retrievals); however, cirrus-impacted pixels, which range from thin cirrus to thick anvils from deep convection, are included for comparison ($\times$ symbols). For boundary layer clouds (circles) and albedo values up to about 0.4, a strong correlation is evident.

the atmospheric scattering phase function are small and (iii) that reflectance at the laser wavelength (532 nm herein) correlates with broadband, solar reflectance.

As global data sets become increasingly available from spaceborne lidar, it will be important to assess the range of validity of these assumptions. A preliminary, direct comparison of πR_L against collocated, satellite-retrieved, broadband albedo from the CERES instrument indicates a strong correlation (r^2, the square of the linear correlation coefficient, is greater than 0.8.) for regions characterized by scattered to broken boundary layer clouds and albedo values up to about 0.4 (see Fig. 2). Thus, πR_L would appear to be a useful albedo proxy for the purposes of this study (i.e. for examining the albedo of thin and broken clouds).

3.2. Lidar reflectivity data sets

We examine distributions of πR_L derived from downward-looking lidars on both airborne and spaceborne platforms. We focus on the mid-visible laser wavelength (532 nm in both cases) because that data is directly tied to a molecular calibration and is most sensitive to scattering by aerosols and thin clouds.

The Cloud Physics Lidar (CPL) is an airborne instrument developed at the NASA Goddard Space Flight Center (McGill

et al., 2002). The two CPL datasets investigated here were acquired at 1 Hz (a horizontal resolution of $\sim$200 m) aboard the ER-2 aircraft flying at an altitude of $\sim$20 km. Figure 3 presents distributions of πR_L acquired by the CPL during two field campaigns: The Observing System Research and Predictability Experiment (THORPEX) (Liu et al., 2004) and the Cirrus Regional Study of Tropical Anvils and Cirrus Layers—Florida Area Cirrus Experiment (CRYSTAL-FACE) (McGill et al., 2004). Flights for THORPEX were conducted above the tradewind marine boundary layer near Hawaii, and those for CRYSTAL-FACE were conducted in the Florida area and over the Caribbean Sea. Both experiments involved partly cloudy conditions. Summaries for both field experiments are given in Table 1.

Figures 3a–c show the frequency distributions of πR_L for the lower troposphere (0–2 km) from both campaigns. To avoid artefacts introduced by signal attenuation, profiles with substantial attenuation above 2 km (presumably from middle and upper level clouds) have been excluded. The CPL data exhibit L-shaped distributions wherein cloudy columns display a wide range of values that merge smoothly into the much narrower range of cloud-free values. There are no indications of a Köhler gap.

Lidar measurements can also be made from space as demonstrated, for example, by the GLAS instrument on NASA's Ice, Cloud and Land Elevation Satellite (ICESat) (Spinhirne et al., 2005). Here again we analyse πR_L from the lower troposphere (0–5 km) and exclude profiles with significant attenuation above 5 km. We use the full-resolution GLAS data, acquired at 40 Hz (175 m resolution). Figure 3d shows the distribution of πR_L from a pass over the Indian Ocean (Hart et al., 2005). This episode involved small cumulus clouds embedded within a marine boundary layer haze and was observed at a time when GLAS laser performance was at its peak. An L-shaped distribution is again evident. In short, for the partly cloudy marine boundary layer, the distributions of measured lidar reflectivity (Figs 3a–d) and simulated albedo (Fig. 1d) look rather similar and indicate a continuum of values, rather than distinct clear and cloudy modes.

4. Causes and extent of albedo continuum

The LES model allows explicit separation of the albedo contributions of activated cloud droplets versus hydrated aerosol and air molecules. Moreover, it permits explicit quantification of the sensitivity of these albedo components to variations in aerosol concentration. Focusing on the partly cloudy ATEX trade cumulus case, we compute albedo over a range of aerosol concentrations by uniformly scaling the number of particles (aerosol and activated droplets) within every grid box while keeping constant the mass of condensed water associated with activated droplets. Thus, we consider only the so-called Twomey effect, also referred to as the 'first indirect aerosol effect.' The scaled aerosol number concentrations range from 75 to 2400 cm^{-3}, which corresponds to dry mass loadings from $\sim$1 to 40 μg m^{-3}, comparable to the observed range from clean to polluted air. Figure 4a

Fig. 3. PDFs of lidar reflectivity at 532 nm for the lower troposphere. CPL measurements at 200 m horizontal resolution during (a) THORPEX and (b) CRYSTAL-FACE projects, (c) CPL measurements at 20 m horizontal resolution obtained during THORPEX on 1 March, 2003, and (d) GLAS measurements at 175 m horizontal resolution obtained over the Indian Ocean. (e and f) Expanded views of albedo continuum region for data shown in (c and d) with contributions of three profile types based on presence or absence of distinct, cloud-like features, as indicated by the maximum value of attenuated backscatter. β' (eq. 2), in each profile. For 'clear' profiles, $\beta'_{max} < 10^{-5}$ m^{-1} sr^{-1}; for 'cloudy' profiles, $\beta'_{max} > 2 \times 10^{-5}$ m^{-1} sr^{-1}; otherwise 'indeterminate.' Numbers in parentheses in (e and f) give number of profiles in each category.
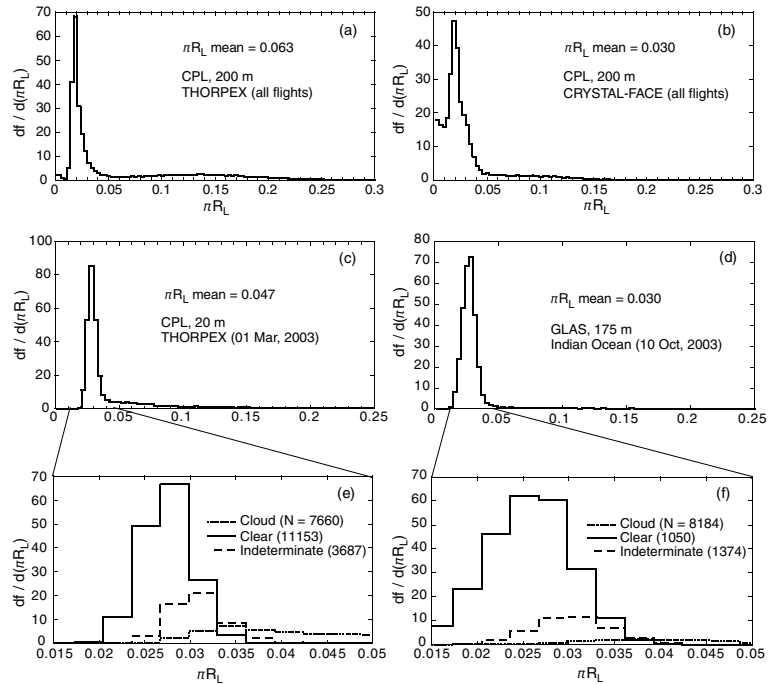
shows albedo PDFs for the total cloud/aerosol/molecular ensemble while Fig. 4b shows albedo PDFs for only the aerosol and molecular components (i.e. excluding extinction by activated droplets). Comparing these figures, we see that at low aerosol concentrations the continuum is attributable to wispy clouds alone, but at high concentrations it is heavily influenced by unactivated, wet aerosol particles. Indeed, these calculations suggest that the humid (but unsaturated) regions between clouds can produce albedos exceeding 0.3 when very high concentrations of hygroscopic aerosol are present.

Lidar measurements provide vertical information that permits an empirical exploration of the causes of the continuum. For the CPL and GLAS cases shown in Figs 3c and d, respectively, we separated the vertical profiles of $\beta'(z)$ (eq. 2) into three categories: those containing distinct cloud-like features (cloudy), those lacking any such feature (clear), and those that could not be categorized (indeterminate). We employed a simple thresh-

old discrimination method based on the maximum value of $\beta'(z)$ after finding that more sophisticated derivative methods did not yield a different result. Profiles in the indeterminate category exhibit peak values of $\beta'(z)$ that cannot unambiguously be identified as either cloudy or clear. As shown in Figs 3e and f, the cloudy and clear profiles have values of πR_L that overlap from about 0.025 to 0.04. According to this analysis, then, the continuum is partly caused by the fact that thick haze and wispy clouds have overlapping values of lidar reflectivity and, by extension from Fig. 2, overlapping values of albedo. An additional factor is the existence of unclassifiable profiles of unknown or ambiguous composition.

Thus, both the lidar and LES model data suggest that the intermediate values of albedo responsible for the albedo continuum are caused by variable mixtures of hydrated aerosol and wispy clouds. Moreover, in many cases, the relative importance of these two factors cannot be determined from remote data

Table 1. Summary of experiments with airborne lidar reflectivity data

Campaign	Region	Location	Dates	Flight hours	Cloud cover[a]
THORPEX	Hawaii (Ocean)	16–41 N 121–167 W	19 Feb–13 Mar 2003	45	42%
CRYSTAL-FACE	Florida and Caribbean Sea	12–30 N 77–87 W	3–28 July 2002	34	17%

[a]Defined here by a combination of backscatter intensity and colour ratio (Liu et al., 2004). These estimates of cloud cover are obtained after excluding all the lidar profiles with features above 2 km that are identified as cloud, which comprise 38 and 81% of the THOREX and CRYSTAL-FACE data, respectively.
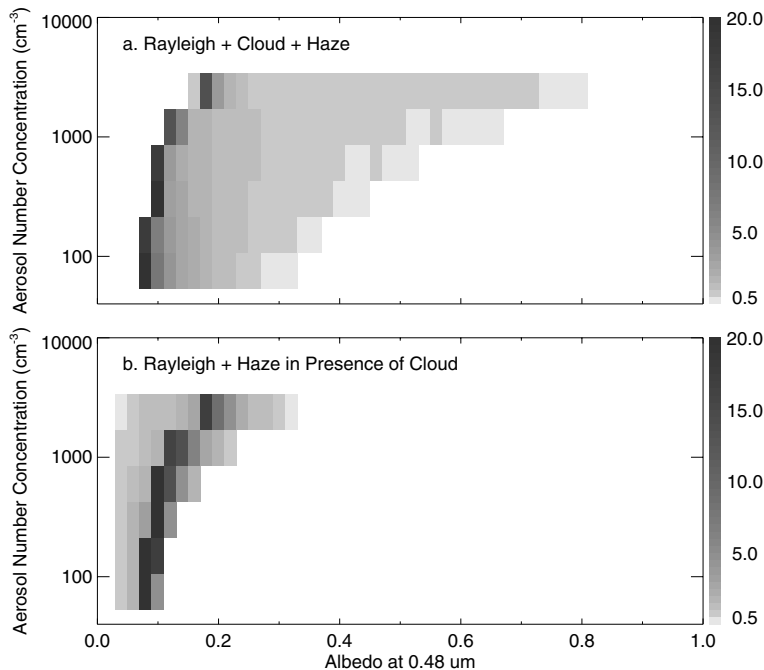
Fig. 4. Albedo PDFs (plotted as d*f*/d*A*) from large-eddy simulations of ATEX trade cumulus over a range of aerosol concentrations. Albedo calculations all based on baseline model simulation with aerosol number concentration of 150 cm^{-3} (further details provided in the text). Albedo distributions at each aerosol concentration use displayed grey scale for (a) total albedo (cloud + aerosol + molecular scattering) and (b) contribution of aerosol haze + molecular scattering only, in presence of cloud. Simply removing clouds would cause an exaggeration by neglecting shading of haze by clouds, which reduces the sunlight reflected by underlying and interstitial haze. To avoid this exaggeration, PDFs in (b) are obtained by first computing albedos for clouds only and then subtracting those albedos from total albedo.

alone—additional, in situ data on aerosol dry mass concentration and relative humidity would be required.

Consistent with many previous studies, these results show that an albedo continuum is likely to be present under partly cloudy conditions. It is worth noting, therefore, that such conditions are extremely common over the global oceans. For example, surface observations (Warren et al., 1988) indicate that scattered-to-broken cloud cover occurs ~70% of the time over the ocean while completely clear skies are rare (<5% of the time, except over the Arctic Sea and the northern Indian Ocean in winter). As another illustration of this problem, in Appendix C we present PDFs of albedo over the ocean from both a general circulation model (GCM) and from CERES measurements averaged to GCM-like resolution (1° × 1°). Consistent with the prevalence of partly cloudy conditions, these PDFs also display an unbroken continuum of albedos, indicating that the global oceans cannot even roughly be separated into clear and cloudy domains when viewed at the resolution of modern GCMs.

5. Consequences for cloud clearing and cloud identification

While the activation of a cloud droplet is unequivocally defined in thermodynamic terms by the Köhler equation, a *cloud* is defined in meteorology as a 'visible aggregation' of particles (Glickman, 2000), regardless of the thermodynamic state of the system. This definition is ambiguous, as has long been recognized in satellite observations of clouds (e.g. Rossow, 1989).

To examine this definitional problem, we use the LES model to calculate changes in cloud cover, F_{cloudy}, resulting solely from changes in aerosol number concentration (N) according to three different cloud-screening algorithms. The liquid water associated with activated droplets (hereafter referred to as cloud water) is held constant in these calculations (described in Appendix A). First, we have developed a thermodynamic-optical algorithm, which is applicable only in a model context but provides a useful reference definition. Under this algorithm, a cloud-containing column is one in which the optical depth of activated droplets, τ_{cloud}, is greater than 0.5 (equivalent to a 30-m thick layer with droplet effective radius of 10 μm and cloud water mixing ratio of 0.1 g kg^{-1}). The other two algorithms attempt to emulate the cloud-screening procedures for the AERONET surface sun photometer network and the MODIS satellite program, respectively. Because remote observations cannot distinguish between thermodynamic states of particles, operational cloud-screening filters must rely on expected radiative features of cloudy air. (We note that underlying surface reflectivity is also commonly included in downward-looking measurements, a further complication that we ignore in our analysis of the LES results.) The AERONET (Smirnov et al., 2000) and MODIS (Martins et al., 2002) cloud-screening filters use the variability of column properties at visible wavelengths to identify clouds. Details of how we emulate these filters are provided in Appendix A. Importantly, the MODIS algorithm operates at a much lower horizontal resolution (~500 m) than the other two.

Figures 5a and b show results for the nearly clear (BOMEX) and the partly cloudy (ATEX) cases, respectively. Three points are noteworthy. First, the three algorithms produce wildly different estimates of F_{cloudy}, illustrating the inherent ambiguity in operational definitions of cloud. Second, F_{cloudy} increases with N
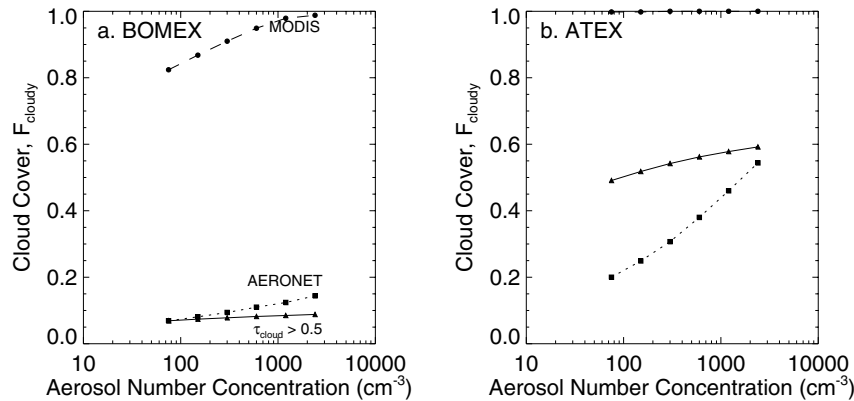
Fig. 5. Cloud cover from large-eddy simulations of (a) BOMEX and (b) ATEX conditions. Cloudy columns defined by three criteria, as denoted in legend: (1) activated cloud droplet optical depth > 0.5; (2) spatial variability of total optical depth (cloud + aerosol + molecular scattering), emulating 'triplet stability criteria' used in AERONET cloud screening algorithm, and (3) spatial variability of 1.5 × 1.5 km regions, emulating '3 × 3-STD' MODIS cloud screening algorithm. AERONET and MODIS cloud-screening emulations are described in the text. Albedos all based on baseline model simulations with aerosol number concentration of 150 cm^{-3}, as in Fig. 4.

for all three algorithms, despite the fact that activated liquid water is held constant. In the case of the thermodynamic-optical algorithm, this is entirely due to the so-called Twomey effect—that is, τ_{AD} increases with N because the cloud water is spread among more droplets, increasing the total surface area of droplets. In turn, F_{cloudy} increases to the extent that columns with a small amount of cloud water cross the threshold of $\tau_{cloud} = 0.5$. Third, the rate at which F_{cloudy} increases with N is much greater for the observational algorithms than for the reference thermodynamic-optical algorithm. For example, the rate of increase is two to four times greater for the AERONET algorithm. This amplification is attributable to the observational algorithms responding not only to the cloud water but also to the optical depth of the unactivated aerosol, which increases rapidly with N. This third point implies that empirical studies of aerosol-induced changes in cloudiness (e.g. Kaufman and Koren, 2006) are likely to find a positive relationship, even in the absence of any aerosol-induced changes in cloud dynamics, simply because of the way that 'cloud' is observationally identified.

6. Consequences for aerosol climate forcing estimates

Current estimates of aerosol climate forcing rely on the conventional expression for albedo (eq. 1) in the sense that 'direct' and 'indirect' aerosol effects are separately calculated for the clear and cloudy portions of Earth (Junge, 1975). This approach would be appropriate if the atmosphere consisted entirely of nearly clear (BOMEX-like) and overcast (ASTEX-like) regions, or if clear and cloudy portions of the atmosphere could be unambiguously separated in a way that did not depend upon aerosol concentration. The existence of partly cloudy regions (ATEX-like) and the fact that the clear-cloudy distinction is ambiguous and aerosol-dependent (as shown above) raise the possibility that the conven-

tional expression may lead to errors. To assess this, we use the LES model to calculate domain-wide albedo as a function of N for all three cases (Fig. 6a). The sensitivity of albedo to changes in aerosol concentrations can then be calculated without the traditional separation into 'direct' and 'indirect' components and without the need to separate the domain into clear and cloudy portions (Figs 6b and c). To gauge potential errors in using the conventional expression, we compare the partly cloudy (ATEX) case to a 50/50 mixture of the nearly clear (BOMEX) and overcast (ASTEX) cases. We display albedo sensitivity in terms of both the local (Fig. 6b) and cumulative (Fig. 6c) derivatives. The former indicates sensitivity to successive doublings of aerosol number while the latter indicates sensitivity to a progressive increase with respect to a low aerosol number (e.g. pre-industrial conditions).

Both the local and cumulative derivatives show the same general result: albedo sensitivity does not depend strongly on N for the conventional approach (represented by the 50/50 mixed case) whereas the sensitivity increases rapidly with N for the partly cloudy case. Thus, the comparison shown in Fig. 6 implies that conventional calculations of aerosol forcing for partly cloudy conditions substantially overestimate the actual forcing at low-to-moderate aerosol concentrations and underestimate the actual forcing at high aerosol concentrations.[1]

The forcing errors implied by Fig. 6 apply to model calculations. In terms of observation-based estimates, we note that those atmospheric states that create the albedo continuum make a substantial contribution to the average albedo in regions of scattered-to-broken skies yet are likely excluded from observational assessments of aerosol effects because they cannot readily be classified as either clear or cloudy. For example, Fig. 4b

---

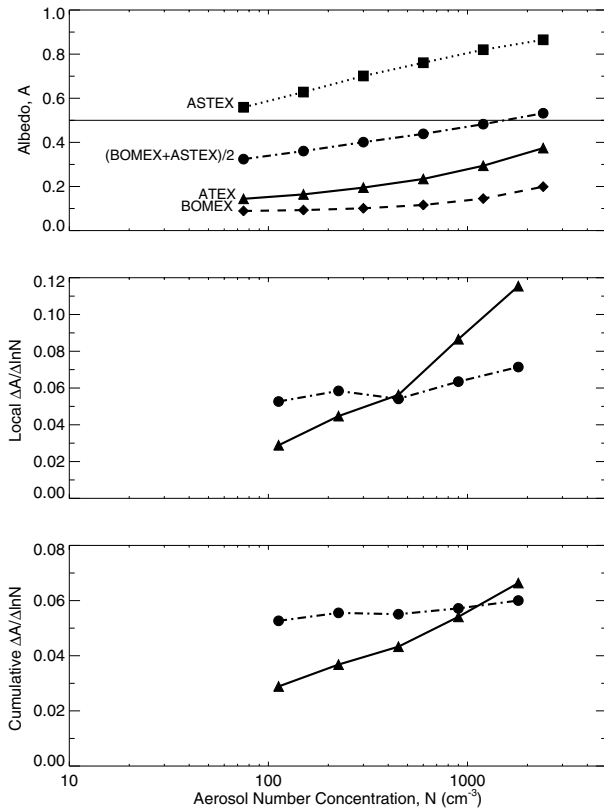[1]We caution that our analysis is limited to one combination of meteorological conditions.

Fig. 6. Average albedo and albedo changes from large-eddy
simulations. Albedos (A) are all based on baseline model simulations
with aerosol number concentration (N) of 150 cm^{-3}, as in Fig. 4: (a)
albedo as a function of N, (b) local derivative of A with respect to a
relative change in N and (c) cumulative derivative of A with respect to a
relative change in N taken with respect to calculations at $N = 75\ cm^{-3}$.
Dashed lines for BOMEX, dotted for ASTEX, dash–dotted for
1/2(BOMEX+ASTEX), and solid for ATEX results.

indicates that, in heavily polluted air, the albedo of unactivated
haze can exceed 0.3, a value comparable to that of modestly thick
cloud. Figures 5a and b indicate that satellite cloud-clearing al-
gorithms based on spatial variability of reflectance are likely to
overestimate cloud cover in such situations and thereby underes-
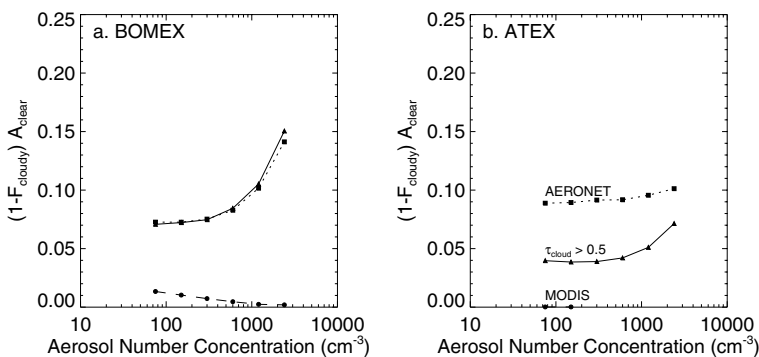timate the areal extent and radiative impact of clear-sky aerosols.

Finally, we consider the dependence of direct aerosol forcing
on cloud definition in Fig. 7. For the nearly clear case (BOMEX),
the forcings for our thermodynamic-optical definition and that
implied by our emulation of the AERONET cloud screening al-
gorithm are comparable. This agreement results from the domi-
nance of the change in aerosol opacity over the change in $(1 -
F_{cloudy})$ for this case, as the changes in aerosol opacity are well
represented by the clear-sky subsets that pass through these two
filters. In contrast, for the broken-sky-cover case (ATEX), the di-
rect aerosol forcings differ substantially between these two cloud
definitions for all but the most polluted conditions. This lack of
agreement is associated with the increased values and absolute
differences of F_{cloudy} for this case (see Fig. 5). For the definition
of cloud implied by the emulated MODIS cloud screening filter,
$(1 - F_{cloudy})$ is substantially smaller than for the other filters in
both meteorological cases, resulting in a drastic underestimation
of the direct aerosol forcing (where it can be defined) compared
to the others.

7. Discussion

Along with previous studies (e.g. Considine et al., 1997), our
results imply the existence of subvisible clouds in the marine
boundary layer. Specifically, large-eddy simulations of partly
cloudy situations indicate that activated droplets occupy much
more area than the highly reflective regions that would nor-
mally be classified as cloudy. Of course, the notion of 'subvisible
clouds' points to an ambiguity in defining a cloud as a 'visible
aggregation' of particles.

The difficulties of defining cloud boundaries and cloud
fractional coverage have long been recognized. For example,
25 years ago Platt and Gambling (1971) used lidar and infrared
radiometer measurements to show that shallow cumulus clouds
often have non-visible haloes of enhanced liquid water extending
for hundreds of metres beyond the visible cloud edge. Twenty
years ago Wielicki and Welch (1986) used high resolution Land-
sat data to show that discrete clouds exist at very small sizes (tens
of metres) and that the measured cloud coverage depends both on
the threshold reflectance used to define cloud and on the spatial
resolution of the sensors. Many recent studies have addressed the
observational problem of subpixel-scale clouds (e.g. Considine

Fig. 7. Direct aerosol forcings computed
from large-eddy simulations of BOMEX and
ATEX conditions using eq. 1, in which
F_{cloudy} from three definitions used to define
'clear' regions is shown in Fig. 5.

et al., 1997; Matheson et al., 2006). What has not been recognized in these previous studies is the important role that aerosol concentration can play in these definitional problems. Clearly, this role needs to be considered when remote observations are used to assess aerosol radiative forcings.

The continuum problem extends beyond the marine boundary layer. Scattered-to-broken sky cover is common over land and has been shown to display similar characteristics (e.g. Wielicki and Welch, 1986). In addition, an albedo continuum in the free troposphere is suggested by the predominance there of very small cloud optical depths reported from satellite-borne lidar (Spinhirne et al. 2005).

These findings lead to several recommendations for future research. First, the rationale for separating cloudy and clear skies in a wide variety of observational databases should be carefully reconsidered. Second, a new approach to quantifying climate forcing by aerosols—focused on the sensitivity of domain-mean albedo to changing aerosol loading—may be required. In other words, the clear-cloud separation required for breaking the problem into 'direct' and 'indirect' components (Junge, 1975) may be an inappropriate starting point. Third, in attempting to quantify albedo sensitivity to increased aerosols, a major challenge is to develop accurate, global-scale knowledge of the distribution of relative humidity in the vicinity of clouds. Satellites cannot as yet provide high-resolution, relative-humidity profiles and model estimates have large uncertainties. Finally, future studies of climate forcing by aerosols should investigate alternatives to the traditional separation of direct and indirect effects. For example, one could attempt to quantify aerosol total radiative forcing for the mixed cloudy-clear system, as in Fig. 6. Grappling with the actual nature of this problem will require an ability to quantify or parametrize the thermodynamic state of water over the entire global atmosphere with considerable detail and fidelity at scales down to tens of metres or fewer, which is no small challenge.

Based upon analysis of lidar data and model simulations, we suggest that the observed continuum in the PDF of albedo (or proxy albedo) is likely to be present in partly cloudy skies, particularly over the ocean, and that it may constitute a significant contribution to global mean albedo. In spite of the seeming impossibility of knowing with sufficient accuracy the relative humidity distribution of the entire atmosphere, particularly in the complex spatial fields associated with broken clouds, a logical first step exists toward assessing the possible importance of the continuum to global albedo. The recent launch of the CALIPSO satellite with its two-wavelength lidar will allow assessment of the fraction of the globe (and its geographic distribution) in an indeterminate state between cloudy and clear skies as in Figs 2e and f. While in situ and suborbital lidar studies will be needed to explore horizontal scales smaller than the CALIPSO resolution of ∼300 m, the realistic possibility of establishing globally the provenance, pervasiveness, and significance of the albedo continuum is now within reach.

8. Acknowledgments

9. Appendix A: Methods

9.1. Large-eddy simulations

The large-eddy simulations use a three-dimensional fluid dynamics model that incorporates a bin microphysics model, which resolves the size distributions of aerosol and cloud droplet concentrations in each grid cell, and a two-stream radiative transfer model that treats the vertical transport of solar and infrared radiative fluxes within each model column (Ackerman et al., 2004). For the trade cumulus simulations the computational domain extends 6.4 km in both horizontal directions and 3 km vertically, with $96 \times 96 \times 96$ cells in the x, y and z directions, respectively. Grid spacing is uniform horizontally and stretched vertically to give cells of height 20 m close to the surface and in the vicinity of the trade inversion. For the stratocumulus simulation the grid extends 3.2 km in both horizontal directions and 1.5 km vertically, with $64 \times 64 \times 86$ cells in the x, y and z directions, respectively, and the vertical grid stretching gives cells of height 6 m close to the surface and in the vicinity of the temperature inversion capping the marine boundary layer. The total particle number concentration at each grid point is fixed in each simulation at $150 \ cm^{-3}$. The aerosol dry size distribution is lognormal with a geometric mean radius of 0.1 μm and a geometric standard deviation of 1.2. Other aspects of the model configuration are described by Ackerman et al. (2004).

The BOMEX trade cumulus simulations are based on an idealization of measurements obtained during the Barbados Oceanographic and Meteorological Experiment as described by Siebesma et al. (2003) and references therein. The ASTEX stratocumulus simulations are based on an idealization of measurements obtained during the Atlantic Stratocumulus Transition Experiment as described by Ackerman et al. (2004) and references therein. The ATEX trade cumulus simulations are based on an idealization of measurements obtained during the Atlantic Trade Wind Experiment (Stevens et al., 2001). Solar radiation for an overhead sun is included in the ATEX simulations to reduce
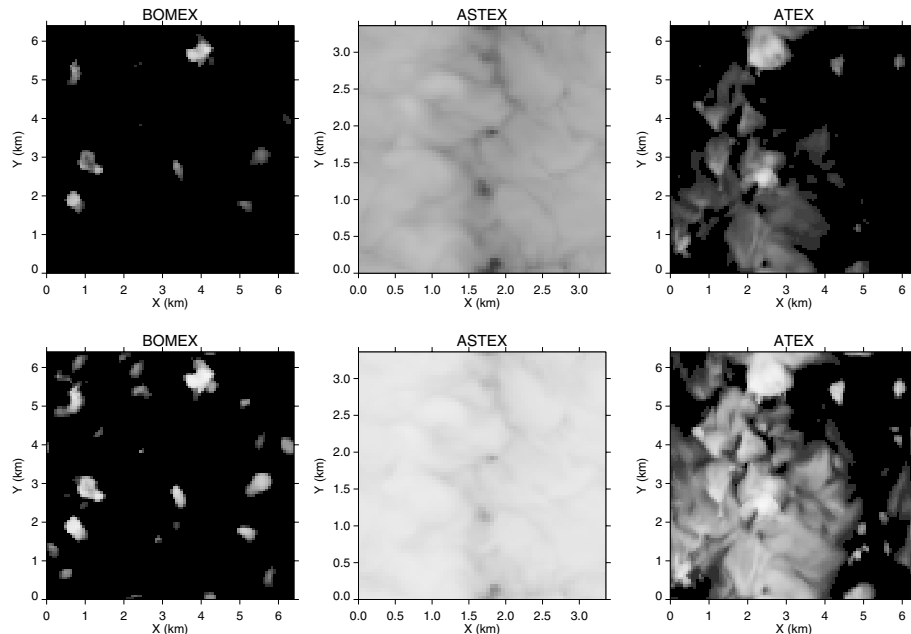
Fig. 8. Albedo at 480 nm wavelength four hours into model simulations based on meteorological conditions from BOMEX, ASTEX, and ATEX. BOMEX is a pure trade cumulus regime, ASTEX is a stratocumulus regime, and ATEX is a transitional trade cumulus regime (with long-lived stratiform anvils that form at the base of a sharp tradewind inversion capping the boundary layer). In the top panels the aerosol number concentration is 150 cm^{-3} and the albedos are computed directly from the simulated model fields. In the bottom panels the same model fields are used, but the aerosol and cloud droplet concentrations are multiplied by 16 and cloud droplet sizes decreased by $16^{1/3}$ to preserve the cloud water distribution.

the fractional cloud cover[2] to ~50%; the other simulations are performed using interactive infrared radiation only.

The trade cumulus simulations are run for four hours and the stratocumulus simulation for eight hours in order to analyse comparable numbers of columns ($>25\,000$ for each simulation). After allowing the turbulence to spin up for two hours for the trade cumulus and three hours for the stratocumulus simulations, the model fields are sampled hourly for offline computations of albedo. Albedo at the top of the atmosphere is computed in a wavelength band centred on 480 nm (with a width of ~40 nm) assuming an overhead sun (solar zenith angle of zero) and that all aerosol and cloud droplets have the optical properties of liquid water. For unactivated aerosol, we incorporate the effect of relative humidity on aerosol size using the Köhler equation (Pruppacher and Klett, 1978) and assuming that each dissolved molecule of solute releases exactly two ions (as for ammonium bisulfate). The albedo calculations are all based on baseline simulations with aerosol concentration of 150 cm^{-3}; albedos computed for aerosol concentrations of (75, 300, 600, 1200 and 2400) cm^{-3} use the same model fields from the baseline simulations but with aerosol and droplet concentrations multiplied by a factor $m = (1/2, 2, 4, 8$ and $16)$ and droplet sizes multiplied by $m^{-1/3}$ to

maintain the same condensed water distributions as in the baseline model fields. Snapshots of the simulated albedo fields are shown in Fig. 8.

Note that we use the independent column approximation in our radiative computations, thereby excluding horizontal radiative transfer, which adds further complications to distinguishing haze from clouds (Wen et al., 2006). Also, our diagnostic treatment of scaling particle concentrations by design omits any dynamical effects of increased aerosol concentrations on cloud properties, which have been shown to result in increased cloud cover in some model studies (Stevens et al., 1998; Ackerman et al., 2003) and decreased cloud cover in others (Jiang and Feingold, 2006; Xue and Feingold, 2006).[3]

9.2. Emulation of cloud screening algorithms

The AERONET cloud screening algorithm (Smirnov et al., 2000) has several stages, and we emulate only one of them, which is the 'triplet stability criterion.' This filter is based on the variability of three optical depth (τ) measurements separated by 30 s in time (thus covering 1 min altogether). The triplet survives the filter for clear sky—and the average value is recorded for the

---

[2]Defined here as the time averaged fraction of columns with water mass mixing ratio in activated drops exceeding 0.05 g kg^{-1} in at least one grid cell.

[3]We note that interpretation of aerosol-induced decreases in cloud cover in the studies of Xue and Feingold (2006) and Jiang and Feingold (2006) is complicated by their basing cloud cover on a threshold of liquid water path rather than optical depth.

triplet—if the range of τ over the three measurements is less than or equal to the larger of 0.02 and $0.03\bar{\tau}$, where $\bar{\tau}$ is the average of the three measurements. We assume an average wind speed of 5 m s^{-1} to convert the spatial variability on our grid to the temporal domain, which we approximate by skipping one grid box to represent 30 s (the grid spacing is $\sim$70 m in our trade cumulus simulations). Although the standard AERONET operational mode is to measure triplets every 15 min, we sample all our model columns to maximize the sample size.

The MODIS cloud screening algorithm (Martins et al., 2002) also has multiple stages, and we emulate only one of them, which is the '3 × 3-STD' cloud mask. This filter is based on the spatial variability of visible reflectance in a 3 × 3 grid of 9 pixels, with each pixel at 500 m resolution. The central pixel survives the filter for clear sky if the standard deviation of reflectance in the nine pixels is less than 0.0025. Instead of reflectance, we use the albedo from a two-stream calculation for an overhead sun. We average the albedo over 8 × 8 grid columns (at $\sim$70 m grid spacing) to approximate the 500 m pixels used in the MODIS cloud mask.

Note that there are further stages of the cloud screening algorithms for AERONET and MODIS that we are not emulating. By emulating only one stage of each cloud screening algorithm (which we understand to be the principal filter in both cases) we allow more of the model domain to be considered clear sky than there would be if we emulated all of the stages. Because our primary point in emulating the cloud screening algorithms is to show how they undersample the data and bias the apparent aerosol radiative forcing, by not emulating all the stages of the cloud screening algorithms we are being generous with respect to the amount (and effects, presumably) of undersampling.

10. Appendix B: Plotting conventions for albedo distribution

A major theme of this paper is exploring the relationship between the albedo of a spatial domain and the variability of albedo within that domain. Here we point out that there are at least two legitimate ways to present the statistical distribution of albedo values. (1) The standard convention is to plot df/dA versus A— that is, normalized frequency versus albedo. This convention allows the relative frequency of albedo values to be seen in proportion to their areal coverage. Thus, one can visually estimate the area-weighted mean albedo of the domain and see what albedo values are controlling that mean. For these reasons, we have employed the standard convention in all probability plots above. (2) An alternate convention is to plot A df/dA—that is, the albedo-weighted frequency—on the ordinate. This convention does not permit an accurate visual estimate of area-weighted mean albedo. However, unlike the standard convention, it properly conveys the relative contributions of various albedo values to the total reflected light. (Thus, for example, regions with zero albedo would disappear from such a plot, even if they represented
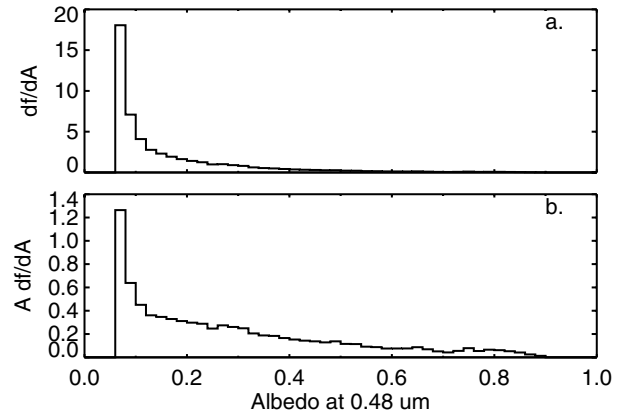

Fig. 9. Comparison of albedo PDF plotting conventions. (a) The standard convention (df/dA versus A) shows the distribution of albedo values over the domain in proportion to their contribution to area-weighted mean albedo. (b) The alternate convention (A df/dA versus A) shows the distribution of albedo values over the domain in proportion to their contribution to total reflected light. In the example above, high albedo regions that appear to contribute negligibly to the albedo distribution when using the standard convention become much more prominent under the alternate convention.

substantial portions of the domain. This is physically appropriate in the sense that such regions make no contribution to reflected light.) Since total reflected light is proportional to albedo, such a plot is directly relevant to assessing what controls the albedo of a given domain. Indeed, the integral of the albedo-weighted function is mathematically equal to the domain-mean albedo:

$$\int_0^1 A \frac{\mathrm{d}f}{\mathrm{d}A} \mathrm{d}A = \bar{A}. \tag{B1}$$

These two plotting conventions are compared in Fig. 9, using data from the ATEX simulation. Panel (a) shows the standard convention, repeated from Fig. 1d. Panel (b) shows the alternate, albedo-weighted convention. High albedo regions that make substantial contributions to reflected light are prominent in panel (b) but virtually invisible in panel (a). Thus, for some applications, it will be preferable to use this alternate convention.

11. Appendix C: Satellite and climate model results

The primary sources of global albedo estimates for the Earth are from broad-band radiometers aboard polar-orbiting satellites, and these data at relatively low resolution are used to provide a fundamental constraint for modern general circulation models (GCMs). Assessments of albedo-related forcings and feedbacks rely on GCMs and, thereby, are rooted in the data from satellites. For the sake of completeness in surveying available information, we consider satellite and GCM derived albedos and thereby evaluate how albedo is distributed according to these
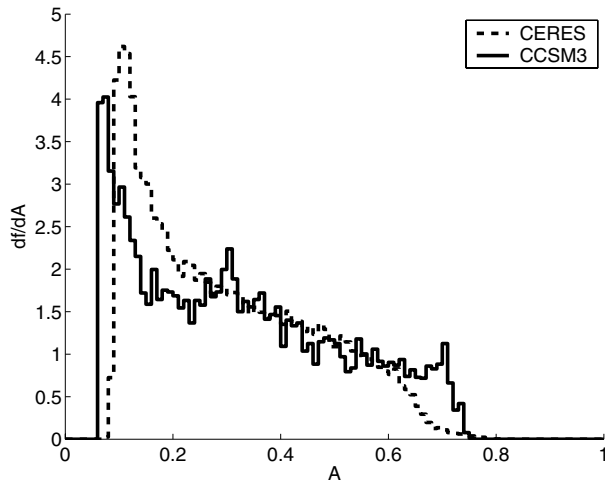
Fig. 10. PDFs of albedo over the global oceans from a satellite radiometer (CERES) and a global climate model (CCSM3). Both sets give broadband albedo (0.3–5 μm for CERES and 0.25–4 μm for CCSM3). Data are omitted poleward of 60° latitude to exclude sea ice. The CCSM3 PDF is based on a global snapshot of the simulated TOA shortwave radiation fields, and the CERES PDF on one day of TOA fluxes. Further details provided in the text.

global-scale assessments and whether these show evidence of an albedo continuum.

Figure 10 shows PDFs of albedo over the global oceans from a CERES instrument (Wielicki et al., 1996; Smith et al., 2004) and from CCSM3, the Community Climate System Model (Collins et al., 2006b). Because our focus is on albedo influences of aerosol and clouds, we examine ocean data only, eliminating what would otherwise be a major source of albedo variation associated with land surfaces.

The CERES data used are derived from instantaneous top-of-atmosphere (TOA) radiance measurements from the CERES Terra Edition 2B Revision 1 Single Scanner Footprint TOA/Surface Fluxes and Clouds product (Loeb et al., 2005). Assuming a constant cloud-scene throughout the day, the instantaneous observations are converted to 24-hr average fluxes through the application of diurnal albedo models, based on angular distribution models described by Loeb et al. (2003). These fluxes are averaged onto a 1° × 1° grid.

The GCM output is a product of the fully coupled Community Climate System Model (CCSM3) (Collins et al., 2006a), run to simulate the present-day climate. The atmospheric component of the model is the Community Atmosphere Model (CAM3) (Collins et al., 2004) and the ocean component is the Parallel Ocean Program (POP) (Large and Danabasoglu, 2006). The model employs a T85 (1.4° × 1.4°) spectral truncation in the atmosphere and a nominal 1° resolution in the ocean.

Both data sets in Fig. 10 show a broad continuum extending from very low albedo (associated with clear skies and scattered, thin clouds) to very high albedo (associated with thick clouds

and overcast conditions). The continuum reflects the fact that subgrid-scale clouds exist over most of the ocean if sampling is performed at a resolution of ∼100 km. The absence of bimodal structure suggests that the global oceans cannot even roughly be separated into clear and cloudy domains when viewed at the resolution of modern GCMs.

References

Ackerman, A. S., Kirkpatrick, M. P., Stevens, D. E. and Toon, O. B. 2004. The impact of humidity above stratiform clouds on indirect aerosol climate forcing. *Nature* **432**, 1014–1017.

Ackerman, A. S., Toon, O. B., Stevens, D. E. and Coakley, J. A. Jr. 2003. Enhancement of cloud cover and suppression of nocturnal drizzle in stratocumulus polluted by haze. *Geophys. Res. Lett.* **30**(7), 1381.

Barker, H. W., Wielicki, B. A., and Parker, L. 1996. A parameterization for computing grid-averaged solar fluxes for inhomogeneous marine boundary layer clouds. Part II: validation using satellite data. *J. Atmos. Sci.* **53**, 2304–2316.

Cess, R. D. 1976. Climate change: an appraisal of atmospheric feedback mechanisms employing zonal climatology. *J. Atmos. Sci.* **33**, 1831–1843.

Charlson, R. J., Langner, J., Rodhe, H. M., Leovy, C. B. and Warren, S. G. 1991. Perturbation of the Northern Hemisphere radiative balance by backscattering from anthropogenic sulfate aerosols. *Tellus* **43AB**, 152–163.

Charlson, R. J., Schwartz, S. E., Hales, J. M., Cess, R. D., Coakley, J. A. Jr., and co-authors. 1992. Climate forcing by anthropogenic aerosols. *Science* **255**, 423–430.

Collins, W. D., Bitz, C. M., Blackmon, M. L., Bonan, G. B., Bretherton, C. S., and co-authors. 2006a. The community climate system model, Version 3. *J. Clim.* **19**, 2122–2142.

Collins, W. D., Rasch, P. J., Boville, B. A., Hack, J. J., McCaa, J. R., and co-authors. 2006b. The formulation and atmospheric simulation of the Community Atmosphere Model version 3 (CAM3). *J. Clim.* **19**, 2144–2161.

Collins, W. D., Rasch, P. J., Boville, B. A., Hack, J. J., McCaa, J. R., and co-authors. 2004. Description of the NCAR Community Atmosphere Model (CAM 3.0). *NCAR/TN-464+STR*, Boulder, CO, USA.

Considine, G., Curry, J. A. and Wielicki, B. A. 1997. Modeling cloud fraction and horizontal variability In boundary layer clouds. *J. Geophys. Res.* **102**, 13517–13525.

Fitzpatrick, M. F. and Warren, S. G. 2005. Transmission of solar radiation by clouds over snow and ice surfaces. Part II: cloud optical depth and shortwave radiative forcing from pyranometer measurements over the Southern Ocean. *J. Clim.* **18**, 4637–4648.

Glickman, T. S. (Ed.): 2000. *The Glossary of Meteorology* 2nd Edition. American Meteorological Society, Boston, MA, USA.

Harshvardhan, B. A., Wielicki, B. A., and Ginger, K. M., 1994. The interpretation of remotely sensed cloud properties from a model parameterization perspective. *J. Clim.* **7**, 1987–1998.

Hart, W. D., Spinhirne, J. D., Palm, S. P. and Hlavka, D. L. 2005. Height distribution between cloud and aerosol layers from the GLAS spaceborne lidar in the Indian Ocean region. *Geophys. Res. Lett.* **32**, L22S03.

Howell, W. E. 1949. The growth of cloud droplets in uniformly cooled air. *J. Meteor.* **6**, 134–149.

Jiang, H. and Feingold, G. 2006. The effect of aerosol on warm convective clouds: aerosol-cloud-surface flux feedbacks in a new coupled large eddy model. *J. Geophys. Res.* **111**, D01202.

Junge, C. E. 1975. The possible influence of aerosols on the general circulation and climate and possible approaches for modelling. GARP Publication No. 16, WMO, Geneva, Switzerland, pp. 244–251.

Kaufman, Y. J. and Koren, I. 2006. Smoke and pollution aerosol effect on cloud cover. *Science* **313**, 655–658.

Köhler, H. 1921. On the condensation of water vapor in the atmosphere (in German). *Geofys. Publ.* **2**.

Köhler, H. 1936. The nucleus in and the growth of hygroscopic droplets. *Trans. Faraday Soc.* **2**, 1152–1161.

Large, W. G. and Danabasoglu, G. 2006. Attribution and impacts of upper-ocean biases in CCSM3. *J. Clim.* **19**, 2325–2346.

Liu, Z., Vaughan, M. A., Winker, D. M., Hostetler, C. A., Poole, L. R., and co-authors. 2004. Use of probability distribution functions for discriminating between cloud and aerosol in lidar backscatter data. *J. Geophys. Res.* **109**, D15202.

Loeb, N. G., Kato, S., Loukachine, K. and Manalo-Smith, N. 2005. Angular distribution models for top-of-atmosphere radiative flux estimation from the Clouds and the Earth's Radiant Energy System Instrument on the Terra Satellite. Part I: methodology. *J. Atmos. Ocean. Tech.* **22**, 338–351.

Loeb, N. G., Smith, N. M., Kato, S., Miller, W. F., Gupta, S. K., and co-authors. 2003. Angular distribution models for top-of-atmosphere radiative flux estimation from the Clouds and the Earth's Radiant Energy System instrument on the Tropical Rainfall Measuring Mission Satellite. Part I: methodology. *J. Appl. Meteor.* **42**, 240–265.

Martins, J. V., Tanré, D., Remer, L., Kaufman, Y., Mattoo, S., and co-author. 2002. MODIS cloud screening for remote sensing of aerosols over oceans using spatial variability. *Geophys. Res. Lett.* **29**(12).

Matheson, M. A., Coakley, J. A. Jr. and Tahnk, W. R. 2006. Effects of threshold retrievals on estimates of the aerosol indirect radiative forcing. *Geophys. Res. Lett.* **33**, L07705.

Matthias, V., Balis, D., Bösenberg, J., Eixmann, R., Iarlori, M., and co-authors. 2004. Vertical aerosol distribution over Europe: statistical analysis of Raman lidar data from 10 European Aerosol Research Lidar Network (EARLINET) stations. *J. Geophys. Res.* **109**, D18201.

Mattis, I., Ansmann, A., Müller, D., Wandinger, U. and Althausen, D. 2004. Multiyear aerosol observations with dual-wavelength Raman lidar in the framework of EARLINET. *J. Geophys. Res.* **109**, D13203.

McGill, M. J., Hlavka, D. L., Hart, W. D., Scott, V. S., Spinhirne, J., and co-author. 2002. Cloud physics lidar: instrument description and initial measurement results. *Appl. Optics* **41**, 3725–3734.

McGill, M. J., Li, L., Hart, W. D., Heymsfield, G. M., Hlavka, D. L., and co-authors. 2004. Combined lidar-radar remote sensing: initial results from CRYSTAL-FACE. *J. Geophys. Res.* **109**, D07203.

Platt, C. M. R. and Gambling, D. J. 1971. Laser radar reflexions and downward infrared flux enhancement near small cumulus clouds. *Nature* **232**, 182–185.

Platt, C. M. R. 1973. Lidar and radiometric observations of cirrus clouds. *J. Atmos. Sci.* **30**, 1191–1204.

Pruppacher, H. R. and Klett, J. D. 1978. *Microphysics of Clouds and Precipitation*. D. Reidel, Dordrecht, The Netherlands.

Ramanathan, V., Cess, R. D., Harrison, E. F., Minnis, P., Barkstrom, B. R., and co-authors. 1989. Cloud-radiative forcing and climate: results from the Earth Radiation Budget Experiment. *Science* **243**, 57–63.

Rossow, W. B. 1989. Measuring cloud properties from space: a review. *J. Clim.* **2**, 201–213.

Siebesma, A. P., Bretherton, C. S., Brown, A., Chlond, A., Cuxart, J., and co-authors. 2003. A large-eddy simulation intercomparison study of shallow cumulus convection. *J. Atmos. Sci.* **60**, 1201–1219.

Smirnov, A. B., Holben, B. N., Eck, T. F., Dubovik, O. and Slutsker, I. 2000. Cloud screening and quality control algorithms for the AERONET database. *Remote Sens. Environ.* **73**, 337–349.

Smith, G. L., Wielicki, B. A., Barkstrom, B. R., Lee, R. B. and Priestly, K. J. 2004. Clouds and the Earth's Radiant Energy System: an overview. *Adv. Space Res.* **33**, 1125–1131.

Spinhirne, J. D., Palm, S. P., Hart, W. D., Hlavka, D. L. and Welton, E. J. 2005. Cloud and aerosol measurements from GLAS: overview and initial results. *Geophys. Res. Lett.* **32**, L22S03.

Stevens, B., Ackerman, A. S., Albrecht, B. A., Brown, A. R., Chlond, A., and co-authors. 2001. Simulations of trade wind cumuli under a strong inversion. *J. Atmos. Sci.* **58**, 1870–1891.

Stevens, B., Cotton, W. R., Feingold, G. and Moeng, C.-H. 1998. Large-eddy simulations of strongly precipitating, shallow, stratocumulus-topped boundary layers. *J. Atmos. Sci.* **55**, 3616–3638.

Trepte, Q., Chen, Y., Sun-Mack, S., Minnis, P., Young, D. F., and co-authors. 1999. Scene identification for the CERES cloud analysis subsystem. *Proceedings of the 10th AMS Conference on Atmospheric Radiation, American Meteorological Society*, Boston, MA, USA, pp. 169–172.

Warren, S. G., Hahn, C. J., London, J., Chervin, R. M. and Jenne, R. L. 1988. Global Distribution of Total Cloud Cover and Cloud Type Amounts over the Ocean. DOE/ER-0406, NCAR/TN-317+STR, Carbon Dioxide Information Analysis Center, Oak Ridge, TN, USA [http://www.atmos.washington.edu/CloudMap].

Wen, G., Marshak, K. and Cahalan, R. F. 2006. Impact of 3-D clouds on clear-sky reflectance and aerosol retrieval in a biomass burning region of Brazil. *Geosci. Remote Sens. Lett.* **3**, 169–172.

Wielicki, B. A. and Welch, R. M. 1986. Cumulus cloud properties derived using Landsat satellite data. *J. Clim. App. Meteor.* **25**, 261–276.

Wielicki, B. A., and Parker, L. 1992. On the determination of cloud cover from satellite sensors: the effect of sensor spatial resolution. *J. Geophys. Res.* **97**, 12799–2823.

Wielicki, B. A., Barkstrom, B. R., Harrison, E. F., Lee, R. B. and Smith, L. 1996. Clouds and the Earth's Radiant Energy System (CERES): an Earth observing system experiment. *Bull. Amer. Meteor. Soc.* **77**, 853–868.

Xue, H. and Feingold, G. 2006. Large-eddy simulations of trade wind cumuli: investigation of aerosol indirect effects. *J. Atmos. Sci.* **63**, 1605–1622.

Zhao, T.-X., Laszlo, I., Minnis, P. and Remer, L. 2005. Comparison and analysis of two aerosol retrievals over the ocean in the Terra/Clouds and the Earth's Radiant Energy System—Moderate Resolution Imaging Spectroradiometer single scanner footprint data: 1. Global evaluation. *J. Geophys. Res.* **110**, D21208.